

X-ray and ultraviolet observations of the dwarf nova VW Hyi in quiescence

Dirk Pandel,¹* France A. Córdoba² and Steve B. Howell²

¹*Department of Physics, University of California, Santa Barbara, CA 93106, USA*

²*Institute of Geophysics and Planetary Physics, Department of Physics, University of California, Riverside, CA 92521, USA*

Accepted 2003 September 1. Received 2003 July 16; in original form 2003 March 3

ABSTRACT

We present an analysis of X-ray and ultraviolet (UV) data of the dwarf nova VW Hyi that were obtained with *XMM-Newton* during the quiescent state. The X-ray spectrum indicates the presence of an optically thin plasma in the boundary layer that cools as it settles on to the white dwarf. The plasma has a continuous temperature distribution that is well described by a power law or a cooling flow model with a maximum temperature of 6–8 keV. We estimate from the X-ray spectrum a boundary layer luminosity of 8×10^{30} erg s⁻¹, which is only 20 per cent of the disc luminosity. The rate of accretion on to the white dwarf is 5×10^{-12} M_⊙ yr⁻¹, about half of the rate in the disc. From the high-resolution X-ray spectra, we estimate that the X-ray emitting part of the boundary layer is rotating with a velocity of 540 km s⁻¹, which is close to the rotation velocity of the white dwarf but is significantly smaller than the Keplerian velocity. We detect a 60-s quasi-periodic oscillation of the X-ray flux, which is likely to be due to the rotation of the boundary layer. The X-ray and the UV flux show strong variability on a time-scale of ~ 1500 s. We find that the variability in the two bands is correlated and that the X-ray fluctuations are delayed by ~ 100 s. The correlation indicates that the variable UV flux is emitted near the transition region between the disc and the boundary layer and that accretion rate fluctuations in this region are propagated to the X-ray emitting part of the boundary layer within ~ 100 s. An orbital modulation of the X-ray flux suggests that the inner accretion disc is tilted with respect to the orbital plane. The elemental abundances in the boundary layer are close to their solar values.

Key words: accretion, accretion discs – binaries: close – stars: dwarf novae – stars: individual: VW Hyi – novae, cataclysmic variables – X-rays: stars.

1 INTRODUCTION

Dwarf novae are powerful X-ray sources with luminosities of 10^{30} – 10^{33} erg s⁻¹. The origin of these X-rays is thought to be the boundary layer between the white dwarf and the inner edge of the accretion disc. There the disc material, initially moving at a Keplerian velocity, dissipates its kinetic energy while being decelerated to the rotation velocity of the white dwarf. The structure of the boundary layer is still an unsolved problem in our understanding of equatorial accretion on to white dwarfs. In the standard picture of dwarf novae, half of the accretion energy is radiated away by the disc, primarily at optical and ultraviolet (UV) wavelengths. Unless the white dwarf is rotating rapidly, the other half of the energy should be liberated in the boundary layer and emitted as X-ray and extreme ultraviolet (EUV) photons. However, observations have shown that for many dwarf novae, the boundary layer luminosity is much lower than the

disc luminosity. In VW Hyi, the X-ray flux during quiescence was found to be a factor of 4 lower than expected in the standard picture (Belloni et al. 1991).

At a distance of 65 pc (Warner 1987), VW Hyi is one of the nearest and brightest cataclysmic variables. It has been studied extensively at optical, UV and X-ray wavelengths. VW Hyi is a dwarf nova of type SU UMa, and it undergoes normal outbursts every ~ 30 d and superoutbursts every ~ 180 d. It has an orbital period of 107 min and lies in a direction with an extremely low hydrogen column density $N_H = 6 \times 10^{17}$ cm⁻² (Polidan, Mauche & Wade 1990). The X-ray spectrum in quiescence is consistent with emission from an optically thin, multi-temperature plasma with temperatures up to ~ 12 keV (Wheatley et al. 1996). van der Woerd et al. (1987) detected coherent soft X-ray oscillations during superoutburst with a period of 14 s and suggested that they originate from the differentially rotating outer layers of the white dwarf or the boundary layer. Sion et al. (2001) inferred that the rotation velocity of the white dwarf projected along the line of sight is 400–500 km s⁻¹, corresponding to a rotation period of ~ 80 s. For our calculations, we assume an

*E-mail: dpandel@xmmom.physics.ucsb.edu

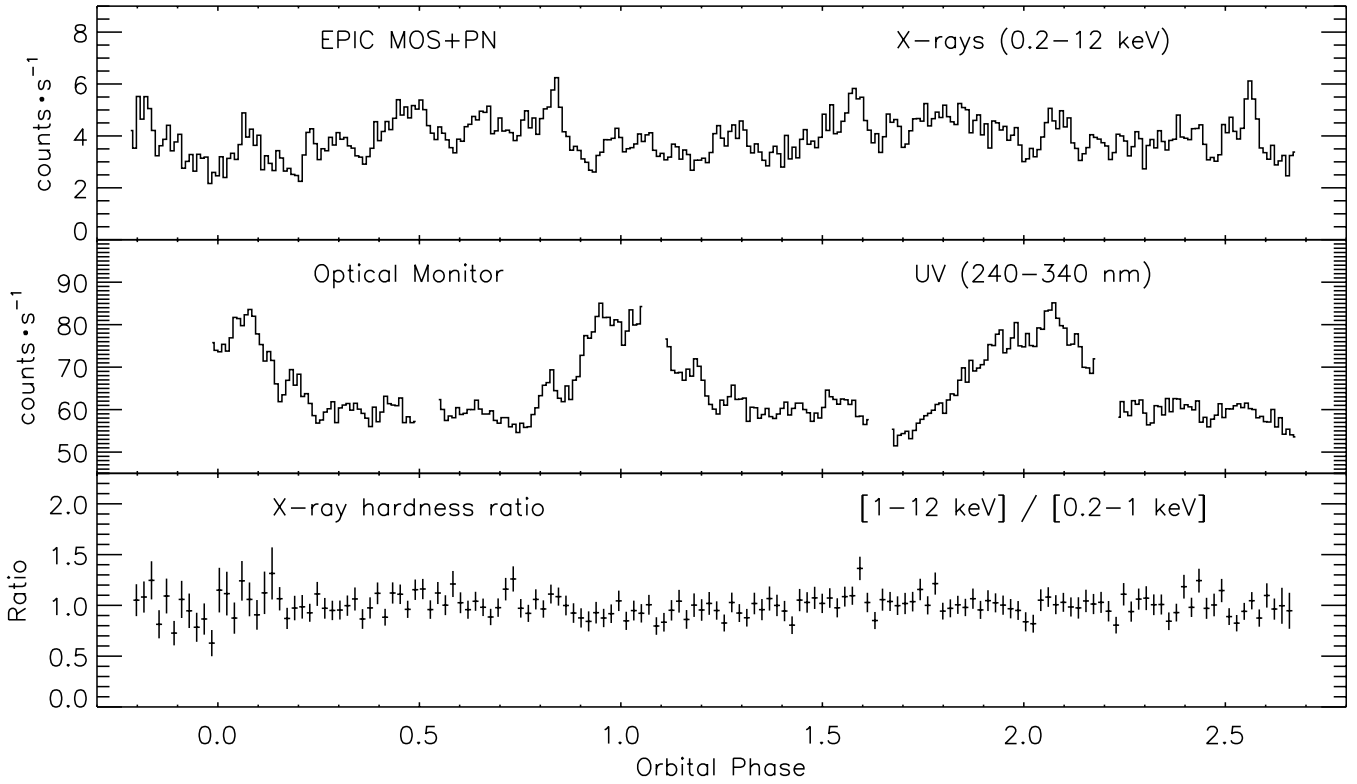


Figure 1. X-ray and UV light curves of VW Hyi obtained with *XMM-Newton* on 2001 October 19 (see Section 3.1). Also shown is the ratio of the count rates in the 1–12 keV and 0.2–1 keV energy ranges. VW Hyi has an orbital period of 107.0 min.

orbital inclination $i = 60^\circ$ (Ritter & Kolb 1998), a white dwarf mass $M_{\text{wd}} = 0.63 M_\odot$ (Schoembs & Vogt 1981), and a white dwarf radius $R_{\text{wd}} = 8.3 \times 10^8$ cm (derived from the mass–radius relationship in Hamada & Salpeter 1961).

In this paper, we present our analysis of *XMM-Newton* data obtained while VW Hyi was in a quiescent state. With the high sensitivity of the X-ray detectors and their broad coverage of the X-ray band, we are able to determine the temperature distribution of the plasma in the boundary layer. We search the X-ray and UV light curves for periodic and quasi-periodic oscillations and characterize the properties of the low-frequency noise (flickering). The capability of *XMM-Newton* for simultaneous X-ray and UV observations enables us to study the correlation between the variability of the boundary layer and the disc luminosity. From the high-resolution Reflection Grating Spectrometer (RGS) spectrum, we infer the rotation velocity of the X-ray emitting plasma in the boundary layer. We derive abundances for elements with strong X-ray emission lines.

2 OBSERVATIONS AND DATA REDUCTION

VW Hyi was observed with *XMM-Newton* (Jansen et al. 2001) on 2001 October 19. At the time of the observation, VW Hyi was in a quiescent state 22 d after a normal outburst and 23 d before a superoutburst [derived from light curves provided by the American Association of Variable Star Observers (AAVSO)]. From the European Photon Imaging Camera (EPIC) instruments (Turner et al. 2001; Strüder et al. 2001), we obtained 18.7 ks (MOS) and 16.1 ks (PN) of continuous X-ray data. The EPIC cameras were operating in small-window mode (MOS) and in full-frame mode (PN). For MOS-1 and PN, the medium blocking filters were selected; for MOS-2, the thin blocking filter was selected. The optical monitor (OM) (Mason et al. 2001) performed five exposures with a total

duration of 16.1 ks using the UVW1 filter (240–340 nm) and one exposure of 1.2 ks using the B filter. The OM was operated in fast mode with a sample time of 0.5 s. We obtained 19.3 ks of data with the RGS (den Herder et al. 2001). Background levels were low during the entire observation.

From the EPIC MOS and PN data, we extracted source photons using a circular aperture with a radius of 40 arcsec. The count rates given in this paper have been corrected for the 88 per cent enclosed energy fraction of this aperture relative to a 60 arcsec aperture (see the *XMM-Newton Users' Handbook*¹). The background rate, which was estimated from larger off-centre regions, contributes less than 1 per cent to the count rate in the source aperture. We included in our analysis good photon events (FLAG = 0) with patterns 0–12 for MOS and 0–4 for PN. To create X-ray light curves, we applied a barycentric correction to the photon arrival times and combined the events from all three EPIC instruments. From the OM fast-mode data, we extracted source photons using a circular aperture of 5-arcsec radius (81 per cent enclosed energy fraction). Sky background contributed ~ 2 per cent to the count rate in the source aperture. The high UV brightness of VW Hyi caused significant coincidence losses at a level of 10–20 per cent. We corrected for these coincidence losses using the method described in the *XMM-Newton Users' Handbook*.

3 TIMING ANALYSIS

3.1 X-ray and UV light curves

Fig. 1 shows background-subtracted X-ray and UV light curves covering three orbital cycles of the binary (orbital period 107.0

¹ http://xmm.vilspa.esa.es/external/xmm_user_support/documentation/uhb/index.html

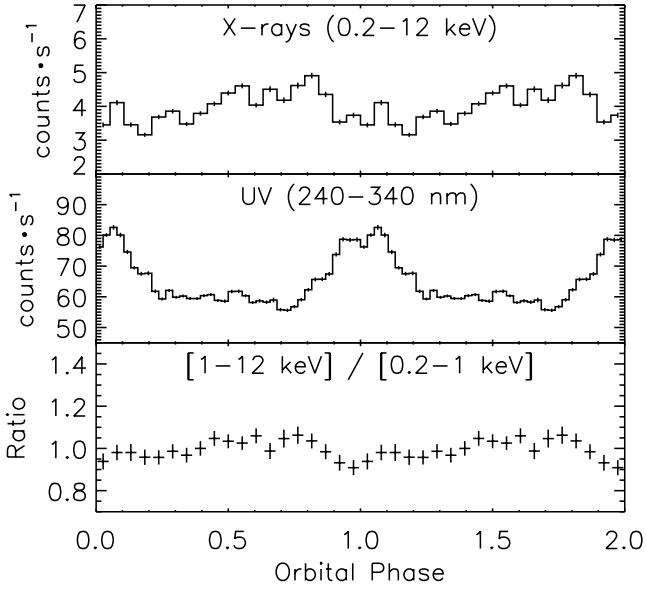


Figure 2. X-ray/UV light curves and X-ray hardness ratio folded on the orbital period of 107.0 min.

min). As orbital phase 0, we selected BJD(TT) 2452201.748, which is the time of peak optical brightness as predicted by the ephemeris in van Amerongen et al. (1987). The ephemeris has an accumulated uncertainty of 250 s or 0.04 in phase. With this choice of orbital phase 0, inferior conjunction of the secondary occurs at ~ 0.27 (Schoembs & Vogt 1981).

The X-ray light curves in Figs 1 and 2 show variability on two time-scales. Clearly visible is an orbital modulation of ~ 30 per cent that is somewhat anticorrelated with the UV flux. The hardness ratio in Fig. 2 indicates that the X-ray spectrum is softer during the fainter part of the orbital cycle. The low-frequency flickering common in dwarf novae is seen as strong flaring with amplitudes

up to ~ 40 per cent and a recurrence time-scale of ~ 1500 s (see Section 3.3). Despite the strong variability of the X-ray flux on this time-scale, the hardness ratio in Fig. 1 remains fairly constant. The average count rate in the 0.2–12 keV energy range is 4.0 s^{-1} .

The UV light curves in Figs 1 and 2 show a strong orbital modulation in the form of a broad hump. This orbital hump is thought to be due to emission from the bright spot, the hot region where the accretion stream from the secondary impacts the outer edge of the disc (e.g. Warner 1995). On time-scales shorter than the orbital period, the UV flux is less variable than the X-ray flux (see Section 3.3 for a statistical analysis). This is to be expected because the UV flux is dominated by emission from the inner accretion disc and the white dwarf, while the X-rays mostly originate from the boundary layer.

In the UVW1 filter, a count rate of 1 s^{-1} corresponds to a flux of $4.5 \times 10^{-16} \text{ erg cm}^{-2} \text{ s}^{-1} \text{ \AA}^{-1}$ at 290 nm. Accordingly, the UV flux from VW Hyi was varying between $2.5\text{--}3.8 \times 10^{-14} \text{ erg cm}^{-2} \text{ s}^{-1} \text{ \AA}^{-1}$ with an average value of $2.9 \times 10^{-14} \text{ erg cm}^{-2} \text{ s}^{-1} \text{ \AA}^{-1}$ or 8.1 mJy. From the short *B*-band exposure (not shown), we estimate that the *B* magnitude was varying between 14.4 and 13.9. Both the UV and the *B*-band brightness ranges agree with past measurements for VW Hyi during quiescence (Pringle et al. 1987; van Amerongen et al. 1987).

3.2 Periodic and quasi-periodic oscillations

Periodograms of the X-ray and UV light curves are shown in Fig. 3. The spectral power is given in Leahy normalization (Leahy et al. 1983), which is suitable for data from photon-counting detectors. In this normalization, the power in each spectral bin has a χ^2 -distribution with 2 degrees of freedom (mean 2 and variance 4), provided that the source is non-variable. The dotted lines in Fig. 3 are the 90 per cent confidence levels for the detection of strictly periodic signals. For frequencies above 0.003 Hz, we do not find any evidence for periodic signals. Although the detection threshold is exceeded below 0.003 Hz, the large spectral power does

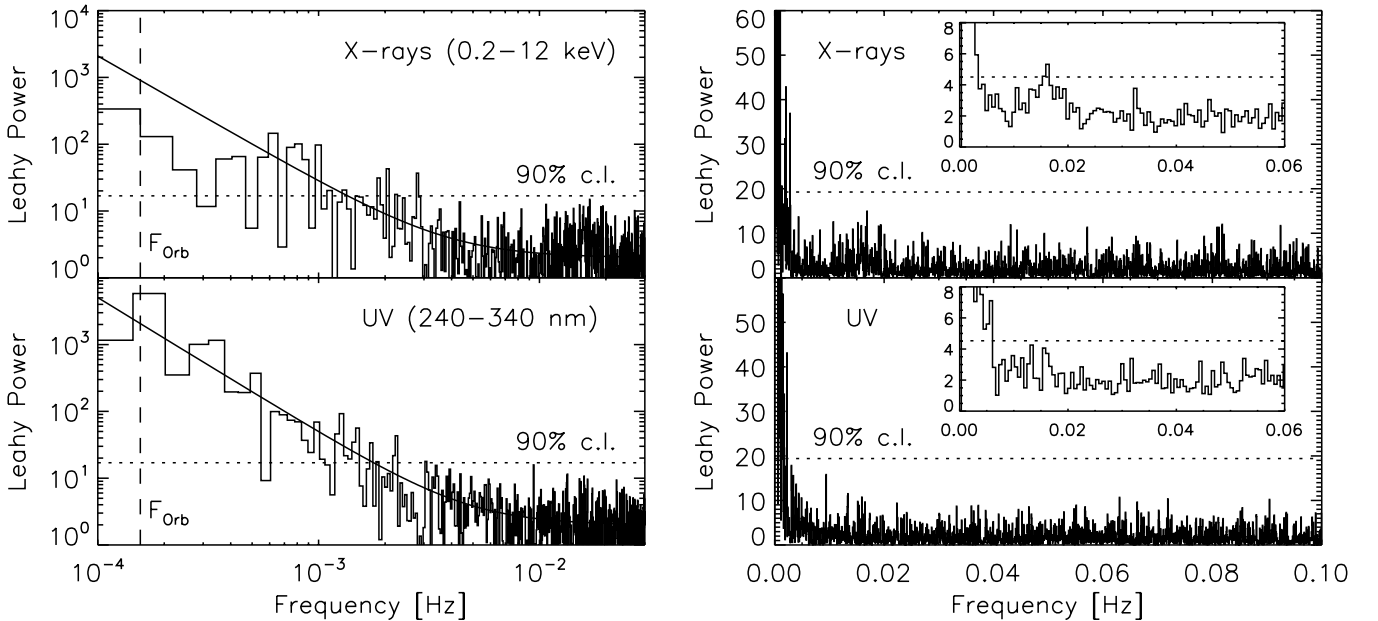


Figure 3. Periodograms of the X-ray and UV light curves shown with logarithmic (left-hand panel) and linear (right-hand panel) scales. The spectral power is given in Leahy normalization, for which each bin has an average value of 2 provided that the source is non-variable and that the observational noise is only due to photon-counting statistics (see Section 3.2). The dotted lines indicate the 90 per cent confidence levels for the detection of strictly periodic signals and the dashed line marks the orbital frequency F_{Orb} . The solid curves show the best fit of a power-law spectral density function. Averaged periodograms obtained by splitting the light curves into 10 equal time intervals are shown in the insets.

not result from periodic signals, but rather from the stochastic process of flickering common in dwarf novae (see Section 3.3). For the frequency range 0.005–1 Hz, we derived upper limits of 3.3 per cent and 0.9 per cent, respectively, for the amplitude of any periodic signal in the X-ray and UV data (confidence level 90 per cent).

To search for quasi-periodic signals, we divided the light curves into shorter time intervals and averaged the periodograms for all intervals. The insets in Fig. 3 show the averages of 10 such periodograms. For the X-ray data, there is a clear excess of spectral power between 0.01–0.02 Hz. Since the power is spread over many frequency bins, the excess does not result from a strictly periodic signal, but rather indicates the presence of a quasi-periodic oscillation (QPO). By summing the spectral power in the frequency range 0.011–0.021 Hz, we find that the QPO is statistically significant at a 6σ level. To estimate the parameters of the QPO, we fitted to the periodogram a spectral density model consisting of a Gaussian plus a constant term for the photon-counting noise using a maximum likelihood method. We obtained a centre frequency of 0.016 Hz (62-s period), a full width at half-maximum FWHM frequency spread of 0.006 Hz (53–77 s period range), and an oscillation amplitude (rms) of 6.2 per cent. To determine the quality of the fit, we simulated spectra with the power density function obtained from the fit by randomizing amplitudes and phases according to the appropriate probability distributions. We find that 96 per cent of the simulated power spectra yield a worse fit than the *XMM-Newton* data.

To further characterize the QPO, we assume that the peak in the power spectrum is caused by a series of random pulses in the light curve that have a Gaussian profile with a sinusoidal modulation. From the above fit results, we can then derive some average properties of these pulses. We obtain a pulse duration of 110 s (FWHM of the Gaussian profile) and $A_p^2/t_p = 0.004 \text{ s}^{-1}$, where A_p is the pulse amplitude in count s^{-1} and t_p is the average pulse separation. A_p and t_p cannot be determined independently, but the non-detection of individual pulses in the light curve requires $A_p \leq 1 \text{ s}^{-1}$ and therefore $t_p \leq 250 \text{ s}$.

The QPO is detected both for hard ($>1 \text{ keV}$) and soft ($<1 \text{ keV}$) X-rays with no apparent difference in strength. However, the QPO is not detected in the UV light curve, which places an upper limit of 0.7 per cent on the rms amplitude in the 0.011–0.021 Hz range. Our periodogram analysis did not reveal any other QPOs in the frequency range 0.02–1 Hz. This places an upper limit of 2.4 per cent for the X-ray data and 0.7 per cent for the UV data on the rms amplitude of any QPO with a frequency spread of 0.01 Hz.

3.3 Flickering and X-ray/UV correlation

At low frequencies, the power spectrum is dominated by the flickering typical for dwarf novae. This low-frequency variability is commonly modelled with a power-law spectral density function $S(f) \propto f^{-\beta}$ (see, for example, Timmer & Koenig 1995). The power-law index β is indicative of the underlying process. For example, random-walk noise has an index $\beta = 2$. We fitted the periodograms with this power-law model plus a constant component for the photon-counting noise. To avoid a bias from the orbital variations at a frequency of 0.000 156 Hz, we restricted the fit to frequencies above 0.0002 Hz. The results of the fits are shown in Fig. 3 (solid curves). We obtained for the power-law index β a value of 1.90 ± 0.19 for the X-ray data and 2.02 ± 0.14 for the UV data. Both indices are consistent with a random-walk noise process. To quantify the strength of the variability, we quote the rms amplitude of the power-law noise above 0.0002 Hz. We obtained an rms of 18 per cent

for the X-ray data and 7 per cent for the UV data. To determine the quality of the fits, we simulated power spectra as described in Section 3.2. We found that 45 per cent of the simulated spectra in X-rays and 93 per cent of the simulated spectra in the UV yield a worse fit than the *XMM-Newton* data. We investigated the dependence of the power-law parameters on the X-ray energy but could not find statistically significant differences between hard and soft X-rays.

At frequencies below $\sim 0.0005 \text{ Hz}$, the X-ray spectral power appears to be lower than predicted by the model fit, indicating that the power law does not continue toward low frequencies. We determined a 99 per cent probability that the low spectral power in the range 0.0002–0.0005 Hz is not a coincidence and is inconsistent with the power-law fit. If frequencies below 0.0005 Hz are excluded from our fit, the power-law index increases to 2.2 ± 0.2 , which is still consistent with $\beta = 2$. The concentration of spectral power around 0.0007 Hz, which gives rise to the strong variability on a $\sim 1500\text{-s}$ time-scale (Fig. 1), may indicate the presence of a QPO. However, the duration of the *XMM-Newton* observation is insufficient to distinguish a QPO from a power-law spectral density function with a changing index β .

To investigate the connection between the X-ray and the UV variability, we calculated the cross-correlation between the two light curves. We removed the obvious correlation on the orbital time-scale by first applying a high-pass filter with a cut-off frequency at 0.0004 Hz. The resulting cross-correlation coefficient as a function of time lag is shown in Fig. 4. A strong peak near zero time lag suggests a significant correlation between the X-ray and the UV variability. The correlation coefficient is normalized such that it has a value of 1 for maximally correlated signals. The high-frequency photon-counting noise introduces a bias that can reduce the correlation coefficient. If we correct for this bias, the peak correlation coefficient increases to 0.5. The central peak is offset with respect to zero time lag, indicating that the X-ray variations are delayed relative to those in the UV by $\sim 100 \text{ s}$. The X-ray/UV correlation disappears when the cut-off frequency of the high-pass filter is increased to 0.001 Hz, demonstrating that the correlation does indeed result from the low-frequency flickering on the 1500-s time-scale. We also investigated the correlation between the hard and soft X-ray variability. We found a strong correlation between the X-ray fluxes above and below 1 keV, but the time lag was consistent with zero to within a few seconds.

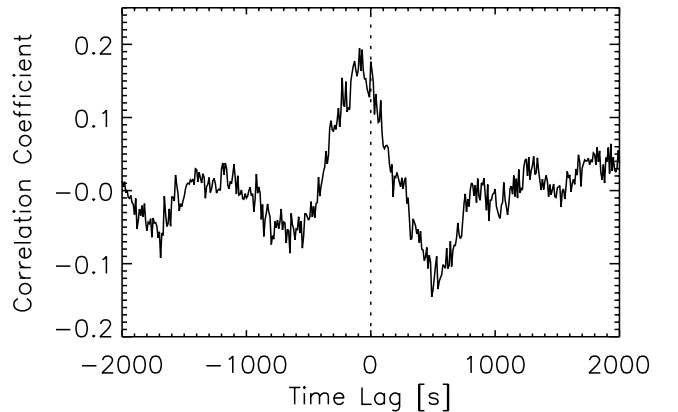


Figure 4. Cross-correlation between X-ray and UV light curves calculated after the variability on time-scales longer than 2500 s had been removed (see Section 3.3). The offset of the central peak with respect to 0 indicates that the X-ray variations lag behind those in the UV by $\sim 100 \text{ s}$.

4 SPECTRAL ANALYSIS

The medium-resolution EPIC spectrum and the high-resolution RGS spectrum are shown in Figs 5 and 6. Both spectra exhibit strong emission lines, indicating the presence of a hot, optically thin plasma. The prominent lines identified by our model fits have been labelled. Spectral fitting was performed with the XSPEC package version 11.2 (Arnaud 1996). As spectral models, we used multi-temperature versions of the MEKAL model, which describes an optically thin, isothermal plasma based on calculations by Mewe, Gronenschild & van den Oord (1985) and Liedahl, Osterheld & Goldstein (1995). For optimal fit results, we binned the EPIC and RGS spectra at one third of the respective FWHM detector resolution. In addition, a minimum of 20 counts per bin were required

for the EPIC spectra so that χ^2 -statistics could be used. To retain the high resolution of the RGS spectra, we did not further rebin the RGS data, but instead accounted for the low number of counts per bin by using C-statistics (Cash 1979).

4.1 EPIC spectrum

The X-ray spectra of dwarf novae in quiescence are commonly fit with one or two single-temperature plasma models. We attempted to fit these models to the EPIC spectra but found that they are inconsistent with the data. However, a good fit could be achieved with a combination of three single-temperature MEKAL models. For the temperatures of the three components, we found 0.5, 1.5 and 5 keV. Adding a fourth component to the model did not improve the fit.

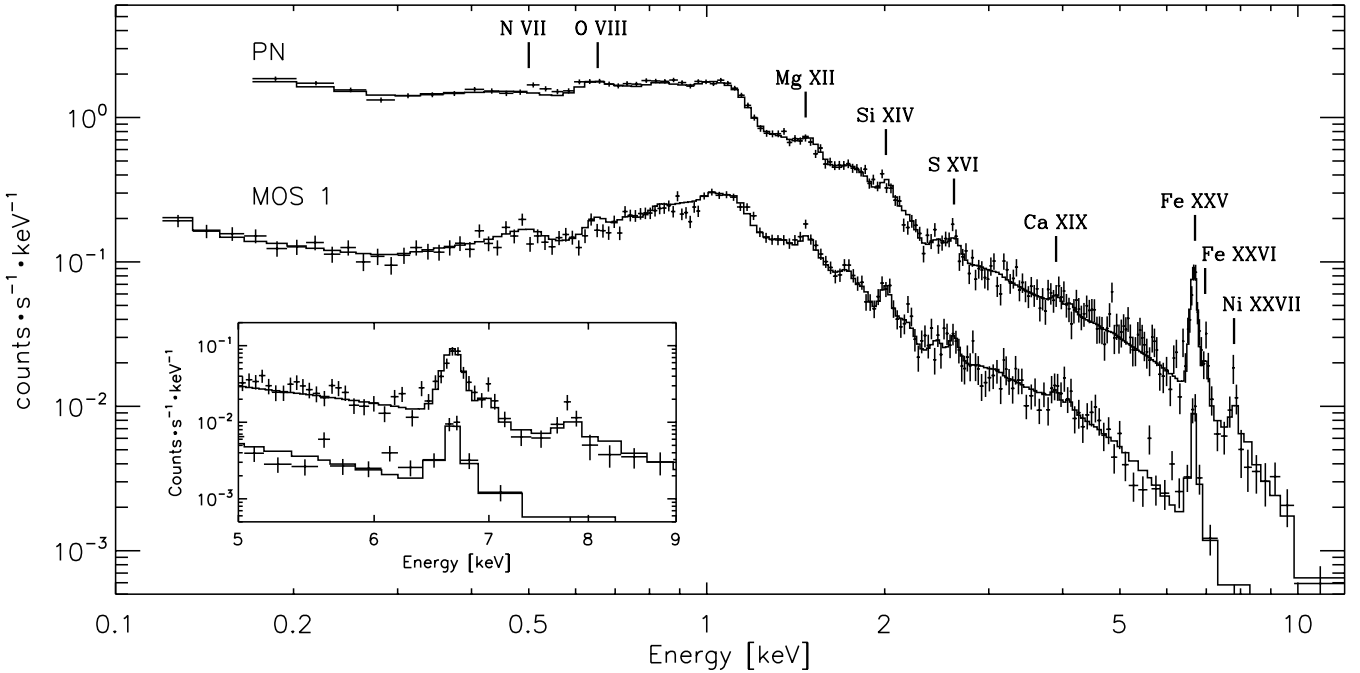


Figure 5. X-ray spectra obtained with the EPIC PN and MOS-1 cameras. Prominent $K\alpha$ emission lines have been labelled. A magnified view of the Fe $K\alpha$ line is shown in the inset. For clarity, the MOS-1 data points have been shifted down by a factor of 2. The solid curves show the best fit with the CEVMKL model (see Section 4.1 and Table 1).

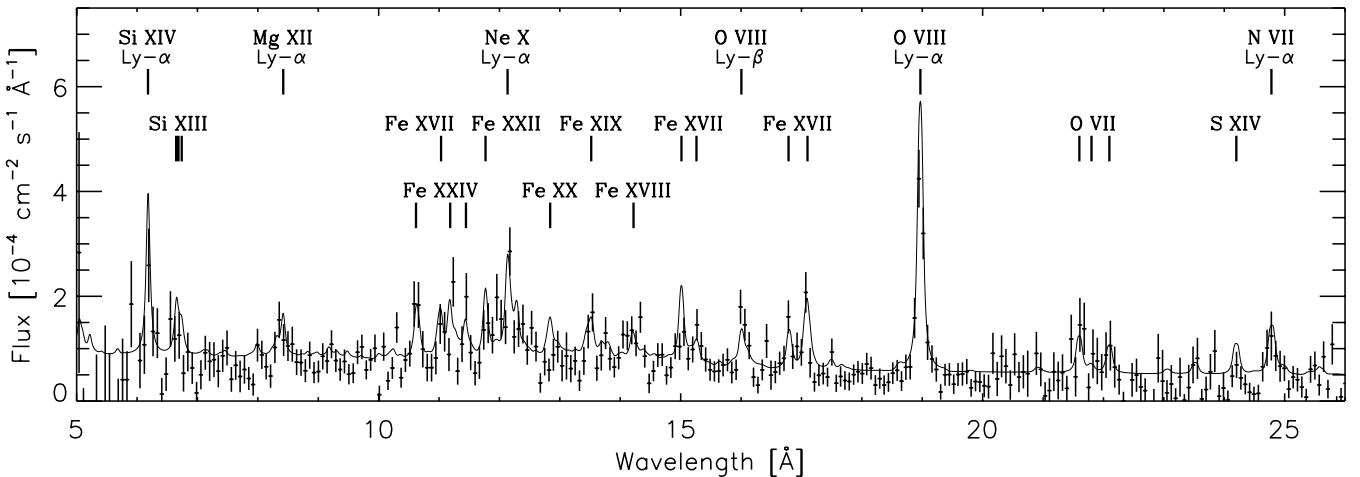


Figure 6. Flux-calibrated RGS spectrum showing the combined first- and second-order RGS-1 and RGS-2 data. Prominent emission lines have been labelled. The solid curve shows the best fit of the CEVMKL model (see Section 4.2 and Table 1). The data is binned at 0.072 Å, the FWHM detector resolution.

Table 1. Results of our spectral fits of various optically thin, multi-temperature plasma models to the EPIC data (see Section 4.1). The CEMEKL and CEVMKL models assume a power-law temperature distribution of the Emission Measure. MKCFLOW is a model for a cooling flow. Except for the CEVMKL model, the abundance ratios were fixed at the solar values given in Anders & Grevesse (1989). For the three PN+MOS fits, the spectra from all three EPIC cameras were fitted simultaneously. In the MKCFLOW model, the fitted low-temperature cut-off kT_{\min} was 0.08 keV (minimum allowed by model). Uncertainties are given at a 1σ level.

Data sets	XSPEC model	Power-law index α	kT_{\max} (keV)	Abundance (solar)	Flux ($\text{erg cm}^{-2} \text{s}^{-1}$)		χ^2 (d.o.f.)	Null hypothesis probability (per cent)
					0.2–12 keV	bolometric		
PN	CEMEKL	1.24 ± 0.04	6.4 ± 0.3	1.03 ± 0.05	6.4×10^{-12}	8.2×10^{-12}	212.1 (185)	8.4
MOS 1	CEMEKL	1.63 ± 0.09	5.3 ± 0.3	0.99 ± 0.08	6.1×10^{-12}	7.4×10^{-12}	280.6 (169)	25.7
MOS 2	CEMEKL	1.38 ± 0.05	5.8 ± 0.3	1.05 ± 0.08	6.4×10^{-12}	8.0×10^{-12}	174.0 (171)	42.2
PN+MOS	CEMEKL	1.35 ± 0.03	6.0 ± 0.2	1.02 ± 0.04	6.3×10^{-12}	8.0×10^{-12}	605.3 (533)	1.6
PN+MOS	MKCFLOW	–	7.8 ± 0.2	0.97 ± 0.04	6.4×10^{-12}	7.8×10^{-12}	616.7 (533)	0.7
PN+MOS	CEVMKL	1.28 ± 0.04	6.2 ± 0.2	see Table 2	6.3×10^{-12}	8.1×10^{-12}	557.3 (521)	13.1

It is evident from this result that the X-ray emitting plasma has a continuous temperature distribution, at least over the range 0.5–5 keV. The multi-temperature nature can be expected for accreting gas that cools as it settles on to the white dwarf. To account for the spread in temperature, we attempted to fit several MEKAL-based continuous-temperature models provided by XSPEC.

The best results were achieved with the CEMEKL model, which fit the data slightly better than the three-temperature model but with a smaller number of parameters. As the simplest of the MEKAL-based multi-temperature models, CEMEKL assumes that the emission measure (EM) has a power-law temperature dependence

$$\frac{dEM}{d \log T} = DEM(T_{\max}) \left(\frac{T}{T_{\max}} \right)^\alpha, \quad (1)$$

where T_{\max} is the maximum temperature of the plasma and $DEM(T_{\max})$ is the differential emission measure at T_{\max} :

$$DEM(T_{\max}) = \left(\frac{dEM}{d \log T} \right)_{T=T_{\max}}. \quad (2)$$

The integration in the CEMEKL code is performed logarithmically (note the $\log T$ above), so that a constant $EM(T)$ corresponds to $\alpha = 1$ (Done & Osborne 1997). The results of our fits are summarized in Table 1. Rows 1–3 show the parameters obtained when the spectrum from each of the three EPIC cameras was fit individually. As can be seen in the null hypothesis probabilities, the CEMEKL model is in very good agreement with the data. The three EPIC spectra yield somewhat different values for the parameters α and T_{\max} . We attribute this to small discrepancies in the cross-calibration of the EPIC detectors. Because the parameters α and T_{\max} are strongly anticorrelated, the differences between the three fits are not as significant as they might appear. Row 4 in Table 1 shows the result for a simultaneous fit of the three EPIC spectra. The null hypothesis probability for the combined fit is significantly lower than for the individual fits, which is a further indication for the cross-calibration discrepancies. Assuming isotropic emission and a distance of 65 pc, we obtain from the fit $DEM(T_{\max}) = 4.3 \times 10^{53} \text{ cm}^{-3}$ at $kT_{\max} = 6.0$ keV. Integrating the power-law model from $T = 0$ to T_{\max} yields a total $EM = 1.4 \times 10^{53} \text{ cm}^{-3}$. The neutral hydrogen column density N_H toward VW Hyi is fairly low at $6 \times 10^{17} \text{ cm}^{-2}$ (Polidan et al. 1990). Accordingly, adding photoelectric absorption to our model did not improve the fit. We derived an upper limit for N_H of $2.2 \times 10^{18} \text{ cm}^{-2}$ (at 90 per cent confidence level).

In the CEMEKL model, the elemental abundance ratios are fixed at solar values and only the total abundance is varied. A significant improvement on the fit could be achieved with the CEVMKL model

Table 2. Elemental abundances derived from our spectral fits with the CEVMKL model (see Sections 4.1 and 4.2). Abundances are given relative to the solar values in Anders & Grevesse (1989). Shown are the best-fitting values and the 90 per cent confidence levels (c.l.). The more reliable abundance estimates are in italics.

Element	EPIC		RGS	
	Best fit	90 per cent c.l.	Best fit	90 per cent c.l.
C	1.5	0.3–2.9	0.82	0.52–1.65
N	1.1	0.0–2.4	1.6	0.9–2.9
O	0.95	0.79–1.12	0.80	0.67–0.91
Ne	0.24	0.0–0.55	0.81	0.29–1.26
Na	>10	>3.4	0.0	0.0–10.4
Mg	1.27	0.91–1.65	0.9	0.4–2.3
Al	4.5	1.6–7.6	0.0	0.0–6.5
Si	1.30	1.05–1.57	2.8	1.6–3.8
S	1.10	0.77–1.45	1.9	0.9–2.9
Ar	0.0	0.0–0.75	4.8	0.2–9.4
Ca	1.8	0.6–2.9	0.0	0.0–3.0
Fe	1.10	0.99–1.22	0.68	0.59–0.77
Ni	2.0	1.1–3.0	0.0	0.0–1.1

(solid curve in Fig. 5 and row 6 in Table 1). In this model, the abundances for the 13 most common elements from C to Ni can be varied independently. Table 2 shows the best-fitting values and the 90 per cent confidence ranges of the abundances obtained with the CEVMKL model. Good constraints are found for the elements O, Mg, Si, S, and Fe, all of which have abundances near the solar values. The abundances are mainly derived from the $K\alpha$ emission line of each element. The most prominent of these lines are labelled in Fig. 5. Because of the lower spectral resolution of the EPIC detectors, confusion of emission lines may bias the measurements for the less abundant elements. In particular, the estimates for Ne and Na are unreliable, since their $K\alpha$ lines lie in the range 0.7–1.3 keV, which is dominated by Fe L-shell lines.

A good fit, though slightly worse than with the CEMEKL model, was achieved with the MKCFLOW model (row 5 in Table 1). MKCFLOW is based on the cooling flow model by Mushotzky & Szymkowiak (1988) and assumes that the emission measure for each temperature is proportional to the inverse of the bolometric luminosity (i.e. proportional to the cooling time). The variable parameters in the model are the minimum and maximum temperatures of the flow (T_{\min} and T_{\max}), the elemental abundance (abundance ratios fixed at solar values) and the flux normalization. The good agreement of the X-ray

spectrum with the MKCFLOW model indicates the presence of hot plasma in the boundary layer that cools as it settles on to the white dwarf. However, the cooling flow model assumes constant pressure and spherical symmetry, which may not be valid in the strong gravitational field of the white dwarf and for the shear and turbulence in a rotating, belt-like boundary layer. Because the CEVMKL model provides the best fit, we will use it in our further analysis.

The maximum plasma temperature of 6–8 keV in VW Hyi is low compared to other dwarf novae. For instance, Mukai et al. (2003) found maximum temperatures of ~ 20 keV for U Gem and ~ 80 keV for SS Cyg, whereas Done & Osborne (1997) obtained ~ 20 keV for SS Cyg. From earlier observations of VW Hyi during quiescence, Hartmann et al. (1999) and Wheatley et al. (1996) derived similarly low temperatures of 10 and 11 keV, respectively, using a cooling flow model. During these observations, however, the X-ray flux was about twice that observed with *XMM-Newton* (see below), which may explain our somewhat lower result of 7.8 keV.

According to our model fits, the bolometric flux from the boundary layer is 8×10^{-12} erg cm $^{-2}$ s $^{-1}$. Because most of the flux is emitted inside the *XMM-Newton* detector band, this estimate is fairly independent of the spectral model (see Table 1). For a distance of 65 pc, the corresponding boundary layer luminosity is $L_{\text{bl}} = 8 \times 10^{30}$ erg s $^{-1}$. Here we assumed that, because of the high orbital inclination, half of the belt-like boundary layer is obscured by the white dwarf. We ignored reflection of X-rays by the white dwarf and a possible obscuration of the boundary layer by the disc. In comparison with previous observations during quiescence, the X-ray flux observed with *XMM-Newton* was about half of that found with *BeppoSAX* (Hartmann et al. 1999), *ROSAT* (Belloni et al. 1991) and *EXOSAT* (van der Woerd & Heise 1987), and about twice that seen with *Einstein* (Cordova, Mason & Nelson 1981). Despite the differences in X-ray flux, VW Hyi had a similar optical brightness during these observations.

To further investigate the orbital modulation of the X-ray flux (Figs 1 and 2), we extracted individual spectra for the bright and the faint parts of the light curve (orbital phases 0.4–0.9 and 0.9–0.4, respectively). We find that the spectrum is softer during the faint phase and that the ratio of faint-phase to bright-phase spectrum is decreasing by ~ 10 per cent from the lowest to the highest X-ray energies. The softening of the spectrum can also be seen in the hardness ratio in Fig. 2. This trend is opposite to what would be expected if the decline in brightness were due to absorption by some intervening gas. Possible causes for the orbital X-ray modulation are discussed in Section 5.4.

4.2 RGS spectrum

The RGS spectrum (Fig. 6) shows a number of prominent emission lines, in particular, the Lyman α lines of some common elements and the Fe L-shell lines between 0.7 and 1.3 keV. As for the EPIC spectra, we fitted the RGS spectrum with the model for an optically thin plasma with a power-law temperature distribution (CEVMKL). Because of the smaller energy range covered by the RGS, the model parameters α and T_{max} were not well constrained. We therefore fixed these parameters at the values obtained from the EPIC spectra ($\alpha = 1.28$ and $kT_{\text{max}} = 6.2$ keV) and only fit the elemental abundances. The best-fitting model is shown as a solid curve in Fig. 6. The elemental abundances (Table 2) are in general agreement with those obtained from the EPIC spectra. The RGS spectrum tends to yield good estimates for elements with prominent Lyman α lines in the RGS detector band (C, O, Ne). For other elements (Mg, Si, S), the Lyman α lines are fairly weak and the more sensitive EPIC detectors

provide better constraints. In Table 2, the more reliable abundance estimates have been highlighted. For most elements, our results are consistent with near solar abundances. We cannot confirm the large overabundance of C and Si found by Huang et al. (1996) for a UV-emitting ring rotating with the Keplerian velocity. However, the UV spectra on which these results are based were obtained 10 days after a superoutburst and the ring may actually be a post-outburst equatorial belt on the white dwarf (Warner & Woudt 2002). The abundances in such a belt may be enhanced due to mixing with the outer layers of the white dwarf. In contrast, our estimates derived from the X-ray spectrum provide the abundances in the accreting gas.

Good estimates from both the RGS and the EPIC spectra were obtained only for the abundances of oxygen and iron. Whereas the two values are consistent for oxygen, there is a noticeable discrepancy for iron. In the EPIC spectrum, the iron abundance is mainly derived from the Fe xxv $K\alpha$ line at 6.7 keV, whereas in the RGS spectrum, the L-shell lines of Fe xvii–xxiv determine the abundance. We interpret the discrepancy for iron as an indication that the power-law model slightly overestimates the emission measure for temperatures at which iron is in the ionization states Fe xvii–xxiv. The model appears to overpredict the strength of the Fe xx line at 12.8 Å and the Fe xvii line at 15.0 Å. The cause for this discrepancy may be a high opacity for these lines. According to Bhatia & Kastner (1999), the Fe xvii line at 15.0 Å weakens significantly relative to the other visible Fe xvii lines for column densities $> 10^{17}$ cm $^{-2}$. For the accretion rate determined in Section 5.3 and for a boundary layer covering 10 per cent of the white dwarf, such a column density can be present if the iron in the cooling gas remains in the Fe xvii ionization state for ~ 5 s.

The width of the O viii line at 19.0 Å is slightly larger than the spectral resolution of the RGS. The likely cause is Doppler broadening due to the rotation of the boundary layer around the white dwarf. Broadening due to the orbital motion of the white dwarf itself is about one order of magnitude smaller and can be neglected. We fitted the line profile assuming that the X-ray emitting part of the boundary layer is a thin equatorial belt near the surface of the white dwarf and found a significantly non-zero rotation velocity $V_{\text{bl}} \sin i = 520$ km s $^{-1}$ with a 90 per cent confidence range of 80–810 km s $^{-1}$. Here i is the orbital inclination of the binary. A slightly better constraint can be obtained by fitting the entire RGS spectrum as described earlier in this section but with the inclusion of the Doppler broadening. We find a best-fitting velocity $V_{\text{bl}} \sin i = 540$ km s $^{-1}$ with a 90 per cent confidence range of 280–810 km s $^{-1}$. This result is in agreement with the rotation velocity of 750 km s $^{-1}$ derived from the 60-s oscillation (see Section 5.1).

5 DISCUSSION

5.1 60-s X-ray oscillation and boundary layer rotation

Coherent dwarf nova oscillations (DNOs) and QPOs have been observed in many dwarf novae at X-ray, UV and optical wavelength (Warner 1995). In VW Hyi, the only X-ray oscillation previously found was a coherent 14-s DNO during superoutburst (van der Woerd et al. 1987). As its origin, the authors suggested the differentially rotating outer layers of the white dwarf or the boundary layer. At optical wavelength, DNOs have been observed in the period range 20–36 s and QPOs have been observed at the periods 23, 88, 253 and 413 s (see table 8.2 in Warner 1995). Recently, Woudt & Warner (2002) found DNOs with a period evolving throughout the outburst from 14 to > 40 s and QPOs with evolving periods of

hundreds of seconds. In all cases, the oscillations were seen during or shortly after an outburst.

The 60-s X-ray QPO we found with *XMM-Newton* is the first oscillation observed in VW Hyi during quiescence. The QPO is detected with equal strength in the soft and hard X-ray bands (i.e. the spectral slope is similar to that of the overall X-ray spectrum), which indicates that the oscillation is caused by small brightness variations in the boundary layer. Emission from a magnetic pole can be ruled out because the oscillation is not strictly periodic. The 60-s oscillation may be related to the rotation of the X-ray emitting gas in the boundary layer. Because VW Hyi is a high-inclination system ($i = 60^\circ$), intermittently brightened parts of the boundary layer may be periodically obscured as they rotate around the white dwarf, thus creating a weakly coherent oscillation. The average lifetime of the brightness fluctuations is ~ 110 s (see Section 3.2), similar to the coherence time of the QPO.

Assuming that the 60-s oscillation is caused by rotation around the white dwarf, we can estimate the rotation velocity of the X-ray emitting gas in the boundary layer. For an orbital inclination $i = 60^\circ$ and a radius equal to the white dwarf radius $R_{\text{wd}} = 8.3 \times 10^8$ cm, we find a rotation velocity $V_{\text{bl}} \sin i = 750$ km s $^{-1}$. This is slightly larger than the velocity of 540 km s $^{-1}$ we determined from the line broadening (Section 4.2) but still within the 90 per cent confidence range. The velocity derived from the QPO may be biased because it depends on the somewhat uncertain values of i and R_{wd} . Our velocity measurements indicate that the boundary layer is rotating significantly slower than the inner accretion disc, which has a Keplerian velocity of ~ 3200 km s $^{-1}$. However, the boundary layer velocity is close to the rotation velocity of the white dwarf $V_{\text{wd}} \sin i = 400\text{--}500$ km s $^{-1}$ determined by Sion et al. (2001) from the width of UV-detected atmospheric lines. It appears that the accreting gas dissipates most of its rotational kinetic energy and decelerates to almost the rotation velocity of the white dwarf before it can radiate efficiently in X-rays.

5.2 X-ray/UV correlation

As discussed in Section 3.3, we found that the variability of the X-ray and UV flux seen on a time-scale of ~ 1500 s is correlated and that the X-ray flux variations are delayed by ~ 100 s. In the past, correlation studies have been rare because of the technical difficulties of simultaneous X-ray and optical/UV observations. With the optical monitor on board *XMM-Newton*, the search for correlations is now greatly simplified. A similar correlation to the one in VW Hyi was found by Jensen et al. (1983) in the nova-like variable TT Ari. There the X-ray variability was also delayed by ~ 1 min.

The observed correlation is somewhat surprising because the X-ray and UV emission originate from distinct regions in the binary. Whereas the source of the X-ray emission is the boundary layer very close to the surface of the white dwarf, the UV flux is emitted by the inner accretion disc (e.g. La Dous 1989) and the white dwarf. Because of the relatively low temperatures, the disc and the white dwarf do not contribute to the X-ray flux. Similarly, the contribution of the boundary layer to the UV flux, as extrapolated from the X-ray spectrum, is only $\sim 3 \times 10^{-4}$ of the total flux.

Because the X-ray flux variations are trailing those in the UV, we can rule out reprocessing of X-rays in the accretion disc as the cause of the correlation. Further investigations of the X-ray data did not reveal noticeable differences between the spectrum during flares and the spectrum between flares. We therefore suspect that the X-ray variability is caused by fluctuations of the accretion rate on to the white dwarf. These fluctuations may be due to accretion rate

variations in the disc, directly seen via the variable UV flux, that propagate inward to the boundary layer. However, the viscous time-scale, i.e. the time-scale for matter to diffuse inward through the disc, is much longer than the observed delay of ~ 100 s (e.g. Frank, King & Raine 1992). The variable UV flux must therefore be emitted from near the transition region between the disc and the boundary layer. There the accreting gas is decelerated well below the Keplerian velocity and is no longer supported by rotation against radial infall. Accretion rate fluctuations near the inner disc edge may be quickly propagated to the inner parts of the boundary layer. Meyer & Meyer-Hofmeister (1994) suggested that, during quiescence, accretion on to the white dwarf does not occur directly from the disc but via a corona that is formed by evaporation of the inner disc. In this model, the UV variability may be connected to variations of the evaporation rate that modulate the amount of gas in the corona and, with some time delay, the accretion rate on to the white dwarf.

As a feasibility test, we estimate the minimum size of the region responsible for the variable UV flux. We assume that the region is emitting as a blackbody and that it is causing the 7 per cent variability of the flux in the UVW1 filter (see Section 3.3). A further constraint on the blackbody can be derived from the non-detection of UV emission at wavelengths shorter than 98 nm (Long et al. 1996). We find a maximum temperature of 3 eV and a minimum emitting area of 6×10^{16} cm 2 . The corresponding width of an annular region with a radius equal to the white dwarf radius R_{wd} is only 0.01 R_{wd} , which is much smaller than the distance from the inner disc edge to the white dwarf (see below). Only a thin annular region near the inner disc edge is needed to produce the variable UV flux.

If our interpretation of the X-ray/UV correlation is correct, the 100-s time delay can provide an estimate for the inner disc truncation radius. The radial infall velocity in the boundary layer is given by $V_r \sim \alpha c_s^2/V_k$ (see e.g. Narayan & Yi 1994), where α is the viscosity parameter, V_k is the Keplerian velocity and $c_s = (kT/\mu m_p)^{1/2}$ is the isothermal sound speed. With the assumption that the temperature in the boundary layer is roughly equal to the initial temperature of the cooling gas $kT_{\text{max}} \approx 7$ keV (Section 4.1), and using $V_k = 3200$ km s $^{-1}$, $\alpha = 0.1$ and a mean molecular weight $\mu = 0.6$, we find an infall velocity $V_r \sim 35$ km s $^{-1}$. The 100-s time delay then suggests that the inner disc edge is $\sim 0.4 R_{\text{wd}}$ above the white dwarf. This result depends on the rather uncertain viscosity parameter α and should only be considered a rough estimate. However, the inner truncation radius cannot be much larger than our estimate because this would be inconsistent with the observed orbital modulation of the X-ray flux (see Section 5.4).

5.3 X-ray luminosity and accretion rate

In quiescence, the combined optical and UV flux from VW Hyi is 1.7×10^{-10} erg cm $^{-2}$ s $^{-1}$, half of which is probably due to the accretion disc (Pringle et al. 1987; Verbunt et al. 1987). For a distance of 65 pc and an inclination of 60° , the corresponding disc luminosity is $L_{\text{disc}} = 4 \times 10^{31}$ erg s $^{-1}$. In Section 4.1, we estimated a boundary layer luminosity $L_{\text{bl}} = 8 \times 10^{30}$ erg s $^{-1}$. In agreement with earlier observations (e.g. Belloni et al. 1991), the ratio of boundary layer to disc luminosity $L_{\text{bl}}/L_{\text{disc}} = 0.2$ is well below the expected value of 1. The cause for this lack of boundary layer emission is still an open question in our understanding of dwarf novae. For VW Hyi, we can rule out a rapidly rotating white dwarf as the cause because the rotation velocity of the boundary layer is much smaller than the Keplerian velocity (see Section 5.1).

As discussed in Section 4.1, the X-ray spectrum is in good agreement with the model of a multi-temperature plasma having a cooling

flow or power-law emission measure distribution. This strongly suggests that the origin of the X-ray emission is cooling plasma in the boundary layer settling on to the white dwarf. The plasma has an initial temperature of 6–8 keV when it begins to radiate efficiently in X-rays. Our results are in remarkable qualitative agreement with the model calculations by Narayan & Popham (1993) for dwarf novae at low accretion rates. The calculations predict the presence of a narrow transition region between the disc and the boundary layer in which the accreting gas is decelerated well below the Keplerian velocity. At this inner disc edge, the gas begins to fall quickly toward the white dwarf and the density decreases by several orders of magnitude. Because of the low density, the gas can no longer cool efficiently and becomes invisible to us. The accreting material continues to dissipate its rotational kinetic energy while being heated to temperatures in excess of 10^8 K. Finally, when the infalling gas is compressed as it piles up on the white dwarf, it begins to cool strongly via bremsstrahlung and becomes visible in X-rays. This compressed, X-ray emitting gas is localized in a thin region on the white dwarf and should be well approximated by a simple cooling flow model. In agreement with our measurements of the boundary layer rotation velocity (Section 5.1), the model calculations predict that the gas in this thin region has been slowed down to almost the white dwarf rotation velocity. However, the model does not explain the low ratio $L_{\text{bl}}/L_{\text{disc}}$.

As the infalling gas is compressed and cools from an initial temperature T_{max} to the much lower white dwarf temperature, it releases an enthalpy $H = 5/2 \times kT_{\text{max}}$ per particle. We can therefore estimate the rate of accretion from the boundary layer on to the white dwarf \dot{M}_{bl} using the relation

$$L_{\text{bl}} = \frac{5}{2} \frac{\dot{M}_{\text{bl}}}{\mu m_{\text{p}}} kT_{\text{max}} \quad (3)$$

(e.g. Fabian 1994). Here μ is the mean molecular weight (typically ~ 0.6) and m_{p} is the proton mass. With an initial temperature $kT_{\text{max}} \approx 7$ keV and a boundary layer luminosity $L_{\text{bl}} = 8 \times 10^{30}$ erg s^{-1} , we find an accretion rate $\dot{M}_{\text{bl}} = 5 \times 10^{-12} M_{\odot} \text{yr}^{-1}$.

For comparison, we estimate the accretion rate in the disc \dot{M}_{disc} from the disc luminosity L_{disc} . With the reasonable assumption that half of the accretion energy is dissipated in the disc, we can calculate \dot{M}_{disc} using the relation

$$L_{\text{disc}} = \frac{GM_{\text{wd}}\dot{M}_{\text{disc}}}{2R_{\text{wd}}} \quad (4)$$

For a white dwarf mass $M_{\text{wd}} = 0.63 M_{\odot}$ and a radius $R_{\text{wd}} = 8.3 \times 10^8$ cm, the disc accretion rate is $\dot{M}_{\text{disc}} = 12 \times 10^{-12} M_{\odot} \text{yr}^{-1}$. Our result seems to indicate that $\dot{M}_{\text{bl}} \approx 1/2 \dot{M}_{\text{disc}}$, i.e. that half of the accreting gas is lost in a wind. A model for such an outflow in dwarf novae during quiescence is described in Meyer & Meyer-Hofmeister (1994). However, our estimate of L_{bl} – and therefore of \dot{M}_{bl} – may be too low if part of the boundary layer is obscured by the disc. The orbital modulation of the X-ray flux (Section 5.4) indicates that at least some obscuration is present. A geometrically thin disc can obscure at most half of the boundary layer so that the actual \dot{M}_{bl} could be up to twice our estimate. It is therefore still possible that $\dot{M}_{\text{bl}} = \dot{M}_{\text{disc}}$ and that no outflow is present. Our estimate of \dot{M}_{disc} may be too low as well if the disc is truncated at a radius significantly larger than R_{wd} . In Section 5.2, we found that the inner disc edge is probably $\sim 0.4R_{\text{wd}}$ above the white dwarf. This would imply that the actual \dot{M}_{disc} is ~ 40 per cent larger than our estimate. However, it seems unlikely that \dot{M}_{disc} can be sufficiently large to attribute the low ratio $L_{\text{bl}}/L_{\text{disc}}$ to a low $\dot{M}_{\text{bl}}/\dot{M}_{\text{disc}}$. In order for \dot{M}_{disc} to satisfy $\dot{M}_{\text{bl}}/\dot{M}_{\text{disc}} = L_{\text{bl}}/L_{\text{disc}} = 0.2$, the inner disc would have

to be truncated at least $\sim 1.0R_{\text{wd}}$ above the white dwarf (or more if we underestimated \dot{M}_{bl}). However, such a large truncation radius is inconsistent with the observed orbital modulation of the X-ray flux (Section 5.4). We conclude that the low boundary layer luminosity L_{bl} cannot be solely attributed to a low accretion rate \dot{M}_{bl} .

The key to understanding the missing boundary layer emission in VW Hyi may be the low initial temperature of the X-ray emitting gas. If the kinetic energy of the material at the inner disc edge, which is rotating at a Keplerian velocity of ~ 3200 km s^{-1} , is converted completely into thermal energy, the plasma would reach a temperature of ~ 21 keV. Yet when the infalling gas first emits X-rays as it piles up on the white dwarf, its temperature is only 6–8 keV. The weak Fe xxvi line at 6.9 keV (see Fig. 5) clearly demonstrates that plasma at higher temperatures is either not present or not radiating efficiently in X-rays. It appears that the gas in the boundary layer loses $\sim 2/3$ of the available accretion energy before it begins to emit X-rays.

It is possible that the gas inside the inner disc edge, where it is decelerated well below the Keplerian velocity, is cooling so rapidly that it cannot reach the maximum temperature of ~ 21 keV. The gas would likely have temperatures higher than the inner disc but not high enough to emit X-rays that could be detected by *XMM-Newton*. However, no strong EUV emission from VW Hyi is observed, and, owing to the low hydrogen column density, not much of the EUV flux can be hidden by interstellar absorption. From the non-detection of EUV emission at wavelengths shorter than 98 nm (Long et al. 1996) and from the quiescent flux detected by *EXOSAT* (Wheatley et al. 1996), we estimate that at most 20 per cent of the expected boundary layer luminosity is emitted in the EUV.

Livio & Pringle (1992) found that a weak magnetic field ($\sim 10^4$ G) of the white dwarf can truncate the inner disc, thus causing the UV delay observed during outburst in some dwarf novae, including VW Hyi. The density inside the inner disc edge may be sufficiently low for the magnetic field to penetrate into the boundary layer and cause the plasma to emit cyclotron radiation. We estimate the cyclotron cooling time-scale t_{cycl} for thermalized, non-relativistic electrons from the emitted cyclotron power (equation 6.7 in Rybicki & Lightman 1979) and find $t_{\text{cycl}}[\text{s}] = 4 \times 10^8 \times B[\text{G}]^{-2}$. For a magnetic field $B = 10^4$ G, the cyclotron cooling time is ~ 4 s, comparable to the infall time of gas not supported by rotation. A significant fraction of the thermal energy could be lost to cyclotron radiation that would be emitted in the radio band. However, strong radio emission from dwarf novae is not observed (e.g. Benz & Guedel 1989). Also, we did not detect strictly periodic X-ray oscillations that would indicate emission from a magnetic pole.

Meyer & Meyer-Hofmeister (1994) suggested that during quiescence, the inner accretion disc evaporates and forms a corona. The gas in the corona is partially accreted on to the white dwarf and partially lost in a wind. The X-ray spectrum is dominated by emission from the cooling plasma piling up on the white dwarf. In this model, some of the thermal energy in the corona is lost to the wind or is conducted back to the accretion disc, which may explain the low temperature of the plasma when it begins to emit X-rays.

5.4 Orbital X-ray modulation

Our investigation of the orbital X-ray modulation showed that the spectrum becomes softer when the flux is decreasing (Section 4.1). This spectral change is opposite to what would be expected if the decline in X-ray flux were due to absorption by some intervening gas (e.g. an extended bright spot). We therefore suggest that the orbital X-ray modulation is caused by a geometric effect, i.e. that, during the faint phase, some hot regions of the boundary layer are blocked from

view, while cooler regions remain visible. For this to be possible, the obscuring material has to be comparable in size and close to the boundary layer (e.g. the white dwarf or the inner accretion disc). We consider the following three possible explanations.

(i) The boundary layer may not be axisymmetric. It is difficult to imagine how an asymmetry that is synchronized with the orbital motion can exist on the rapidly rotating white dwarf. One possibility is asymmetric accretion caused by a non-axisymmetric inner disc. Again, it is unclear how such an asymmetry in the disc could persist for several orbital cycles. In some dwarf novae, stationary structures have been observed in the form of spiral waves (e.g. Steeghs 2001), albeit only during outbursts and in the outer parts of the disc.

(ii) The boundary layer may be partially obscured by a non-axisymmetric inner disc. Because the transition from optically thick disc to optically thin boundary layer is quite abrupt (Narayan & Popham 1993), the disc essentially acts like a circular aperture, blocking part of the X-ray emission. The fraction of visible boundary layer should remain constant, yet it may vary with orbital phase if the inner edge of the disc is not circular. Again, it is unclear what the cause of such an asymmetry might be.

(iii) The rotation axes of the white dwarf and the inner disc may not be aligned. It is thought that the boundary layer forms a belt-like structure on the white dwarf. Because the X-ray emitting part of the boundary layer is mostly corotating with the white dwarf, it is likely to be aligned with the equator. If the inner disc is tilted with respect to the equator of the white dwarf, the fraction of boundary layer obscured by the disc may vary with phase, causing an orbital modulation of the X-ray flux.

In the third scenario, it is unlikely that the rotation axis of the white dwarf is tilted with respect to the orbital plane, because any such misalignment would disappear on a time-scale of 100 yr (Kopal 1978). However, warping of the accretion disc may cause a tilt of the inner disc edge. Murray & Armitage (1998) found that tidal interactions are too weak to cause warping during the high state, but a tilt may be present in the quiescent disc of short-period dwarf novae. Lai (1999) suggested that warping of the inner disc may be caused by a weak magnetic field of the primary. The precession of a warped disc in VW Hyi could be revealed if future observations show a phase shift of the orbital X-ray modulation relative to the orbital hump seen in the UV.

6 CONCLUSIONS

We have analysed *XMM-Newton* data of the dwarf nova VW Hyi obtained during quiescence. The spectrum indicates that the X-ray emission is due to an optically thin plasma that cools as it settles on to the white dwarf. The cooling plasma has an initial temperature of 6–8 keV when it first emits X-rays. This temperature is well below the ~ 21 keV expected if all the rotational kinetic energy of the material in the inner disc were instantly converted into heat. Apparently, the accreting gas loses $\sim 2/3$ of its thermal energy before it piles up on the white dwarf and begins to radiate efficiently in X-rays. We estimated 8×10^{30} erg s $^{-1}$ for the luminosity of the boundary layer, which is only 20 per cent of the accretion disc luminosity. The low boundary layer luminosity cannot be explained by a low mass transfer rate. We derived 5×10^{-12} M $_{\odot}$ yr $^{-1}$ for the accretion rate on to the white dwarf and 12×10^{-12} M $_{\odot}$ yr $^{-1}$ for that in the disc. We determined elemental abundances for some common elements and found no large deviations from the solar values.

From the Doppler broadening of emission lines, we determined that the X-ray emitting part of the boundary layer is rotating with a

velocity $V_{\text{bl}} \sin i = 540$ km s $^{-1}$, which is similar to the white dwarf rotation velocity but much smaller than the Keplerian velocity of the inner disc. This result rules out a rapidly rotating white dwarf as the cause of the low boundary layer luminosity. We found a 60-s quasi-periodic X-ray oscillation with a coherence time of only ~ 100 s. The oscillation is likely caused by the rotation of the boundary layer. The corresponding rotation velocity $V_{\text{bl}} \sin i = 750$ km s $^{-1}$ is consistent with that derived from the line broadening.

The low-frequency variability of the X-ray and the UV flux is well described by a power-law spectral density function with an index consistent with a random-walk noise process ($\beta = 2$). In X-rays, the variability is caused by fluctuations of the accretion rate on to the white dwarf. We found a correlation between the X-ray and the UV variability with the X-ray fluctuations being delayed by ~ 100 s. This result suggests that the variable UV flux is originating from near the transition region between the disc and the boundary layer and that accretion rate fluctuations in this region are propagated to the X-ray emitting part of the boundary layer within ~ 100 s. We estimated from the 100-s time delay that the accretion disc is truncated $\sim 0.4 R_{\text{wd}}$ above the white dwarf. An orbital modulation of the X-ray flux suggests that the inner accretion disc is tilted relative to the equator of the white dwarf and the orbital plane. This warping of the inner disc may be due to a weak magnetic field of the white dwarf.

ACKNOWLEDGMENTS

This work is based on observations obtained with *XMM-Newton*, an ESA science mission with instruments and contributions directly funded by ESA Member States and the USA (NASA). The authors acknowledge support from NASA grants NAG5-7714 and NAG5-12390.

REFERENCES

- Anders E., Grevesse N., 1989, *Geochim. Cosmochim. Acta*, 53, 197
 Arnaud K. A., 1996, in Jacoby G. H., Barnes J., eds, *ASP Conf. Ser. Vol. 101*, Astronomical Data Analysis Software and Systems V. Astron. Soc. Pac., San Francisco, p. 17
 Belloni T. et al., 1991, *A&A*, 246, L44
 Benz A. O., Guedel M., 1989, *A&A*, 218, 137
 Bhatia A. K., Kastner S. O., 1999, *ApJ*, 516, 482
 Cash W., 1979, *ApJ*, 228, 939
 Córdova F. A., Mason K. O., Nelson J. E., 1981, *ApJ*, 245, 609
 den Herder J. W. et al., 2001, *A&A*, 365, L7
 Done C., Osborne J. P., 1997, *MNRAS*, 288, 649
 Fabian A. C., 1994, *ARA&A*, 32, 277
 Frank J., King A., Raine D., 1992, *Cambridge Astrophysics Series*, *Accretion Power in Astrophysics*. Cambridge Univ. Press, Cambridge
 Hamada T., Salpeter E. E., 1961, *ApJ*, 134, 683
 Hartmann H. W., Wheatley P. J., Heise J., Mattei J. A., Verbunt F., 1999, *A&A*, 349, 588
 Huang M., Sion E. M., Hubeny I., Cheng F. H., Szkody P., 1996, *AJ*, 111, 2386
 Jansen F. et al., 2001, *A&A*, 365, L1
 Jensen K. A., Middleditch J., Grauer A. D., Horne K., Gomer R., Córdova F. A., Mason K. O., 1983, *ApJ*, 270, 211
 Kopal Z., 1978, *Astrophys. Space Sci. Lib.*, *Dynamics of Close Binary Systems*. Riedel, Dordrecht
 La Dous C., 1989, *A&A*, 211, 131
 Lai D., 1999, *ApJ*, 524, 1030
 Leahy D. A., Darbro W., Elsner R. F., Weisskopf M. C., Kahn S., Sutherland P. G., Grindlay J. E., 1983, *ApJ*, 266, 160

- Liedahl D. A., Osterheld A. L., Goldstein W. H., 1995, *ApJ*, 438, L115
Livio M., Pringle J. E., 1992, *MNRAS*, 259, 23p
Long K. S., Blair W. P., Hubeny I., Raymond J. C., 1996, *ApJ*, 466, 964
Mason K. O. et al., 2001, *A&A*, 365, L36
Mewe R., Gronenschild E. H. B. M., van den Oord G. H. J., 1985, *A&AS*, 62, 197
Meyer F., Meyer-Hofmeister E., 1994, *A&A*, 288, 175
Mukai K., Kinkhabwala A., Peterson J. R., Kahn S. M., Paerels F., 2003, *ApJ*, 586, L77
Murray J. R., Armitage P. J., 1998, *MNRAS*, 300, 561
Mushotzky R. F., Szymkowiak A. E., 1988, in Fabian A. C., ed., *Cooling flows in clusters and galaxies*. Kluwer, Dordrecht, p. 53
Narayan R., Popham R., 1993, *Nat*, 362, 820
Narayan R., Yi I., 1994, *ApJ*, 428, L13
Polidan R. S., Mauche C. W., Wade R. A., 1990, *ApJ*, 356, 211
Pringle J. E. et al., 1987, *MNRAS*, 225, 73
Ritter H., Kolb U., 1998, *A&AS*, 129, 83
Rybicki G. B., Lightman A. P., 1979, *Radiative Processes in Astrophysics*. Wiley Interscience, New York
Schoembs R., Vogt N., 1981, *A&A*, 97, 185
Sion E. M., Cheng F., Szkody P., Gänsicke B., Sparks W. M., Hubeny I., 2001, *ApJ*, 561, L127
Steeghs D., 2001, in Boffin H. M. J., Steeghs D., Cuypers J., eds, *Astrotomography – Indirect Imaging Methods in Observational Astronomy*. Springer-Verlag, Berlin, p. 45
Strüder L. et al., 2001, *A&A*, 365, L18
Timmer J., Koenig M., 1995, *A&A*, 300, 707
Turner M. J. L. et al., 2001, *A&A*, 365, L27
van Amerongen S., Damen E., Groot M., Kraakman H., van Paradijs J., 1987, *MNRAS*, 225, 93
van der Woerd H., Heise J., 1987, *MNRAS*, 225, 141
van der Woerd H., Heise J., Paerels F., Beuermann K., van der Klis M., Motch C., van Paradijs J., 1987, *A&A*, 182, 219
Verbunt F., Hassall B. J. M., Pringle J. E., Warner B., Marang F., 1987, *MNRAS*, 225, 113
Warner B., 1987, *MNRAS*, 227, 23
Warner B., 1995, *Cambridge Astrophysics Series, Cataclysmic Variable Stars*. Cambridge Univ. Press, Cambridge
Warner B., Woudt P. A., 2002, *MNRAS*, 335, 84
Wheatley P. J., Verbunt F., Belloni T., Watson M. G., Naylor T., Ishida M., Duck S. R., Pfeffermann E., 1996, *A&A*, 307, 137
Woudt P. A., Warner B., 2002, *MNRAS*, 333, 411

This paper has been typeset from a $\text{\TeX}/\text{\LaTeX}$ file prepared by the author.